

A STUDY ON AERODYNAMIC DESIGN OF HIGH-EFFICIENCY PROPELLERS AT HIGH-ALTITUDE

Jianhua Xu, Wenping Song & Wenqing Yang
National Key Laboratory of Aerodynamic Design and Research, Northwestern Polytechnical University, Xi'an, China

Keywords: *high-altitude propeller, aerodynamic design, tandem configuration, RANS equations*

Abstract

The density of air at high-altitude is extremely low. Therefore, one of the main characteristics of flow around propellers at high-altitude is low Reynolds number, resulting in low efficiency of propeller. A Reynolds-averaged Navier-Stokes (RANS) solver on a chimera grid system for both conventional and tandem configuration propellers are developed. Then, an aerodynamic optimization platform for propellers is established by using an efficient optimization method including the genetic algorithm (GA) and the Kriging model. A tandem configuration propeller is formed based on the optimized conventional two-bladed configuration, and the flow around the tandem configuration propeller is investigated, as well as the corresponding aerodynamic performance. The results demonstrated that the efficiency of rear propeller is much lower than that of front propeller for a tandem configuration, whereas the efficiency of the whole configuration is increased.

1 Introduction

Electric energy, transformed by solar energy, is the main energy source for propulsion system and control system on high-altitude aircrafts such as airships and long endurance unmanned aerial vehicles. High efficiency of propulsion system results in less solar cell panel and more effective load. Therefore, the aerodynamic efficiency of propellers has significant influence on the flight performance of these aircrafts. Thus, investigations on flow characteristics around high-altitude propeller and the

aerodynamic design have been get more and more attention. On the other hand, propeller with tandem configuration is widely used in many underwater vehicles such as submarines. Thus, this unconventional configuration is investigated in present research.

In recent thirty years, many research institutes had made many efforts on high-altitude propellers. Colozza[1] made an overview of high-altitude propeller design and analysis, and concluded that low Reynolds number and high subsonic Mach number is the main flow characteristics of a high-altitude propeller, compared to conventional aeronautic propeller. Then, APEX[2][3] vehicle is designed in order to investigate the unique aerodynamic problem. The University of Illinois at Urbana-Champaign (UIUC) developed series of low speed and low Reynolds number airfoils, and also obtained the corresponding experimental data of Reynolds number from 30000 to 500000[4][5][6]. Test in the UIUC subsonic wind tunnel performed by Brandt and Selig documented tests on several low Reynolds number propellers. The results showed significant Reynolds number effects with degradation in aerodynamic performance with lower rotational speed[7].

In present work, a platform for the aerodynamic optimization design of high-altitude propeller with conventional configuration is established based on RANS solver with chimera grid methodology as an analysis method and GA with Kriging model as optimization method. In addition, the aerodynamic performance of propellers with tandem configuration at high-altitude is studied.

2 RANS Solver for Flow around Propellers

In this paper, the velocity of the free stream is assumed to perpendicular to the propeller disk, and the flow around propellers is quasi-steady in the rotational frame fixed to propeller blades. Thus, RANS equations in rotational frame are iterated to steady solution. On the other hand, the chimera grid systems including background grid and blade grid are utilized to convenient for grid generation and implementation of periodic boundary condition.

2.1 RANS equations in Rotational Frame

The integral form of Reynolds-Averaged Navier-Stokes (RANS) equations expressed in the blade-attached rotational frame can be written as follows:

$$\frac{\partial}{\partial t} \iiint_{\Omega} \mathbf{Q} dV + \iint_{\partial\Omega} \mathbf{F} \cdot \mathbf{n} dS - \iint_{\partial\Omega} \mathbf{F}_v \cdot \mathbf{n} dS + \iiint_{\Omega} \mathbf{G} dV = 0 \quad (1)$$

where

$$\mathbf{Q} = \begin{bmatrix} \rho \\ \rho u \\ \rho v \\ \rho w \\ \rho E \end{bmatrix}, \quad \mathbf{F} = \begin{bmatrix} \rho(\mathbf{q} - \mathbf{q}_b) \\ \rho u(\mathbf{q} - \mathbf{q}_b) + p\mathbf{I}_x \\ \rho v(\mathbf{q} - \mathbf{q}_b) + p\mathbf{I}_y \\ \rho w(\mathbf{q} - \mathbf{q}_b) + p\mathbf{I}_z \\ \rho H(\mathbf{q} - \mathbf{q}_b) + p\mathbf{q}_b \end{bmatrix} \quad (2)$$

and

$$\mathbf{F}_v = \begin{bmatrix} 0 \\ \tau_{xx}\mathbf{I}_x + \tau_{xy}\mathbf{I}_y + \tau_{xz}\mathbf{I}_z \\ \tau_{xy}\mathbf{I}_x + \tau_{yy}\mathbf{I}_y + \tau_{yz}\mathbf{I}_z \\ \tau_{xz}\mathbf{I}_x + \tau_{yz}\mathbf{I}_y + \tau_{zz}\mathbf{I}_z \\ \lambda_x\mathbf{I}_x + \lambda_y\mathbf{I}_y + \lambda_z\mathbf{I}_z \end{bmatrix}, \quad \mathbf{G} = \begin{bmatrix} 0 \\ \rho(\boldsymbol{\omega} \times \mathbf{q})_x \\ \rho(\boldsymbol{\omega} \times \mathbf{q})_y \\ \rho(\boldsymbol{\omega} \times \mathbf{q})_z \\ 0 \end{bmatrix} \quad (3)$$

where, t is time, Ω and $\partial\Omega$ stand for control volume and the corresponding boundary, respectively. dS and dV are elemental area and volume of the control volume, respectively. \mathbf{n} is the outward unit normal. \mathbf{Q} is the conservation fluid variables. \mathbf{F} and \mathbf{F}_v are the inviscid and viscous flux term, respectively. \mathbf{G} is the Coriolis force term. Moreover, ρ is density, $\mathbf{q}=[u, v, w]^T$ denotes velocity of flow field, E and H is total energy and enthalpy per unit mass, respectively. \mathbf{q}_b is the moving velocity of cell boundary, p is pressure. $(\mathbf{I}_x, \mathbf{I}_y, \mathbf{I}_z)$ stands for unit vector of Cartesian coordinates. τ and λ denote viscous

stress tensor and heat conduction, respectively. $\boldsymbol{\omega}$ is rotational speed.

The cell-centered finite-volume method with central scheme as spatial discretization scheme[8] is used to solve the above governing equations. An improved Newton-like LU-SGS method[9] is utilized for time stepping and a very efficient FAS multi-grid method[10] on chimera grid is developed to improve the computational efficiency. Turbulence models, including Baldwin-Lomax (B-L) algebraic model[11], Spalart-Allmaras (S-A) model[12] and Menter's $k-\omega$ shear-stress-transport (SST) model[13], are implemented for turbulence enclosure. It should be noted that full turbulent assumption is implemented in present work.

2.2 Chimera Grid System and Boundary Conditions

2.2.1 Chimera Grid System for a Propeller with Conventional Configuration

A Chimera grid system for conventional configuration propeller blade based on two grids in the simulation is involved and demonstrated in Fig. 1, including the background grid and the blade grid, both of which moving with the rotary blade. The background grid (H-H type) is for far-field computation and implementation of periodic boundary condition point by point conveniently. The blade grid (C-H type) shown in Fig. 2 is for viscous flow simulation. There are hole points and fringe points on background grid, shown in Fig. 3 and Fig. 4. The connection and information exchange between background grid and blade grid are implemented by a very efficient and robust method based on a distance decreasing method[14].

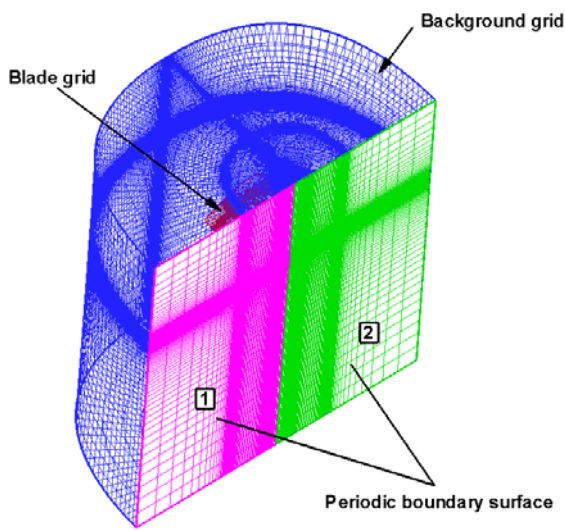


Fig. 1. Chimera Grid System for Conventional Configuration

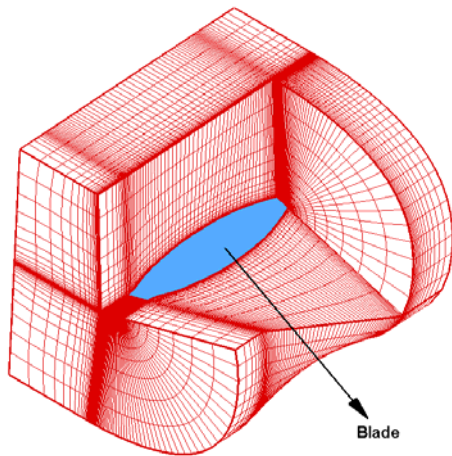


Fig. 2. Cutaway View of C-H Type Blade Grid

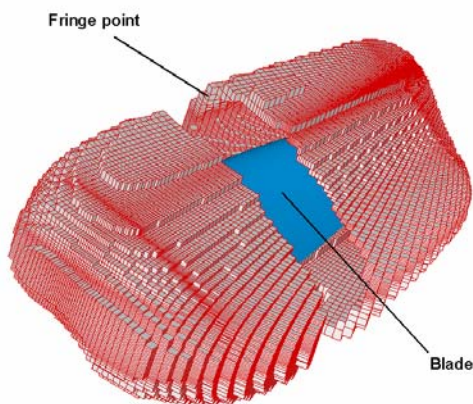


Fig. 3. Overall Schematic Diagram of Fringe Points and Blade

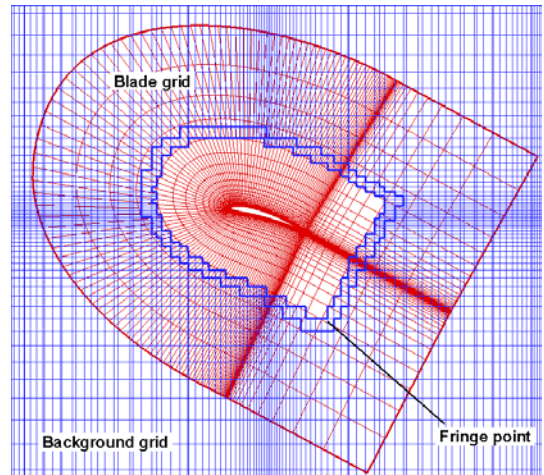


Fig. 4. Cross Section View of Fringe Point on Background Grid

2.2.2 Chimera Grid System for a Propeller with Tandem Configuration

The tandem configuration in this work consists of front blade and rear blade with the same rotational speed and direction each other, shown in Fig. 5. The chimera grid system for a tandem configuration is demonstrated in Fig. 6, and the hole cutting view is illustrated in Fig. 7. It is shown that there are two holes on background grid, and each hole for front blade grid and rear blade grid, respectively.

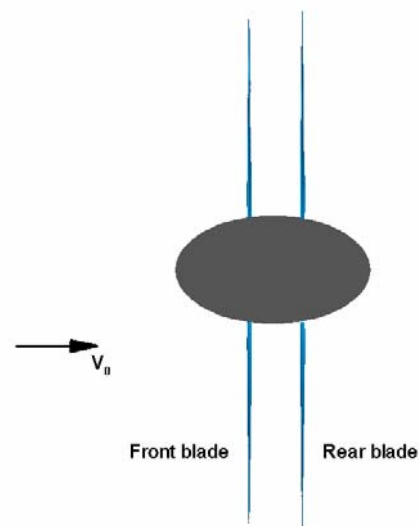


Fig. 5. Tandem Configuration Propeller

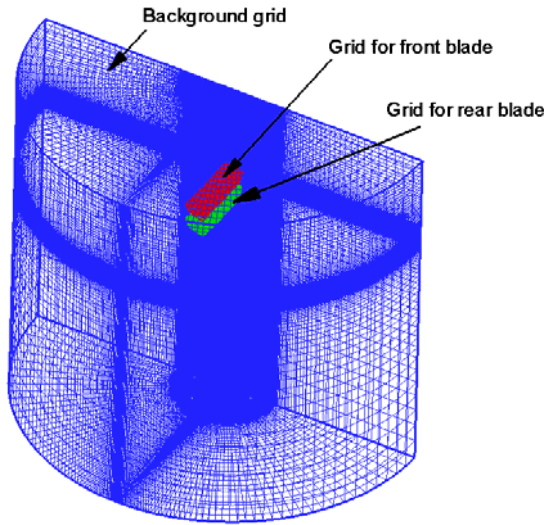


Fig. 6. Chimera Grid System for Tandem Configuration

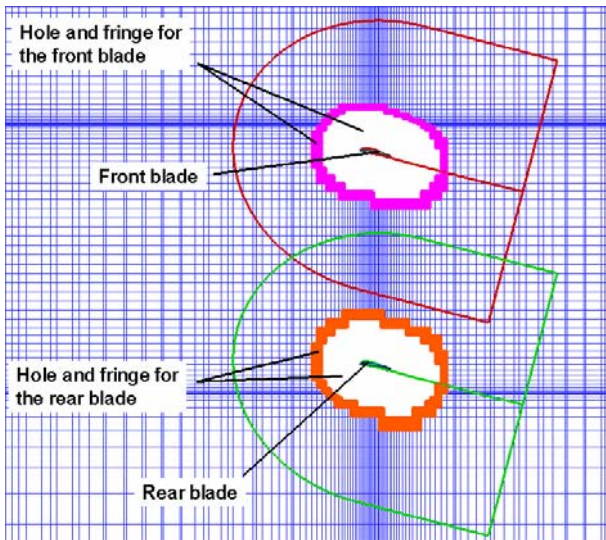


Fig. 7. Cross Section View of Hole Cutting on Chimera Grid System for Tandem Configuration

2.2.3 Boundary Conditions

For viscous flow, no-slip boundary condition and adiabatic wall condition are enforced on the blade surface, i.e. the velocities on the blade surface mesh are consistent with the blade motion. One-dimensional approximate Riemann boundary conditions are applied at far-field boundaries. A trilinear interpolation method[15] is used to calculate the flow variables on fringe points on background grid and chimera boundary points on blade grid. The periodic boundary conditions in Fig. 1 are implemented as follows:

$$\begin{aligned}
 p_1 &= p_2 \\
 \rho_1 &= \rho_2 \\
 \begin{bmatrix} u_2 \\ v_2 \\ w_2 \end{bmatrix} &= \begin{bmatrix} \cos\left(\frac{2\pi}{N_b}\right) & 0 & -\sin\left(\frac{2\pi}{N_b}\right) \\ 0 & 1 & 0 \\ \sin\left(\frac{2\pi}{N_b}\right) & 0 & \cos\left(\frac{2\pi}{N_b}\right) \end{bmatrix} \begin{bmatrix} u_1 \\ v_1 \\ w_1 \end{bmatrix} \quad (4)
 \end{aligned}$$

where, N_b is the number of blades in one propeller disk. It should be noted that conservation variables are used to implement the interpolation process in present research.

3 Aerodynamic Optimization Design for Conventional Configuration Propellers

In this research, the sectional airfoils are fixed through the optimized process. Thus, the class function / shape function transformation (CST) parameterization method[16][17] is used to parameterize the distribution functions both for chord length and twist angle. Then, the in-house high-efficient optimization tool based on GA with surrogate models[18] is presented in this section.

3.1 A Modified CST Parameterization for Propeller Blades

The parameterization is implemented on the effective part of propeller blade, i.e. the relative radius r/R range from 0.2 to 1.0. Thus, for convenient, we use a normalize radius x_r instead of relative radius, shown in Fig. 8. Similar to airfoils, the distributions of chord length and twist angle are parameterized by using a modified CST formulation as following:

$$y = C(x_r) \bullet S(x_r) + x_r \bullet y(1) + (1 - x_r) \bullet y(0) \quad (5)$$

where, y denotes chord length or twist angle, respectively. The last term in equation (5) is an additional one, which is different from airfoil with leading edge. As design variables, $y(0)$ and $y(1)$ are the corresponding values at blade root and tip, respectively.

$C(x)$ is the class function:

$$C(x) = x^{N1}(1-x)^{N2} \quad (6)$$

where, for airfoil shapes, although the exponents $N1$ and $N2$ are recommended as

constants by Kulfan[16][17], they are used as design variables to extend the design space in present paper.

$S(x)$ is the shape function:

$$S(x) = \sum_{i=0}^N A_i \cdot S_i(x) \quad (7)$$

$$S_i(x) = \frac{N!}{i!(N-i)!} x^i (1-x)^{N-i}$$

where, $s_i(x)$ is Bernstein polynomial and A_i is coefficients as design variables.

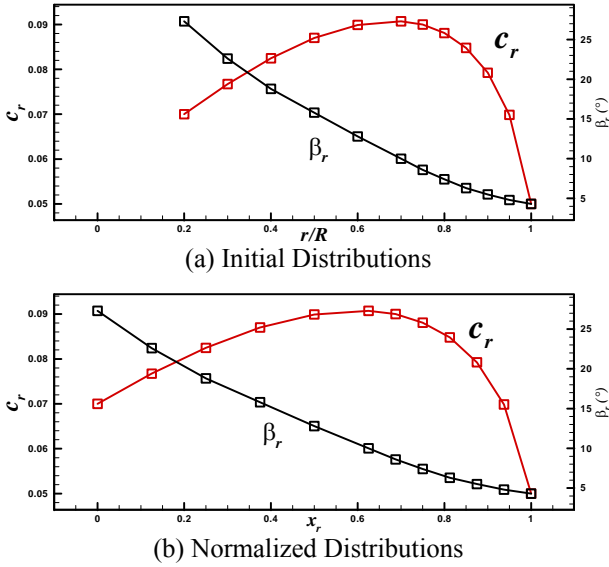


Fig. 8. Distributions of Chord Length and Twist Angle

3.2 Efficient Optimization Method

An in-house high-efficient optimization tool based on GA with surrogate models is utilized. First, several initial sample points are generated in the design space using design of experiments (DoE). Here, we use the Latin hypercube sampling (LHS); then the samples are observed with parallel computing to save total clock time; after that, the Kriging models are constructed both for objective function and constraints (geometry constraints excluded), then the Kriging models are refined repetitively by infilling one or more new points obtained with GA under some specified infill criteria; this iteration terminates until some stop criteria meet, for instance, the function evaluation budgets or expected improvement (EI) exceeds the specified value. The framework of the optimization is as follows:

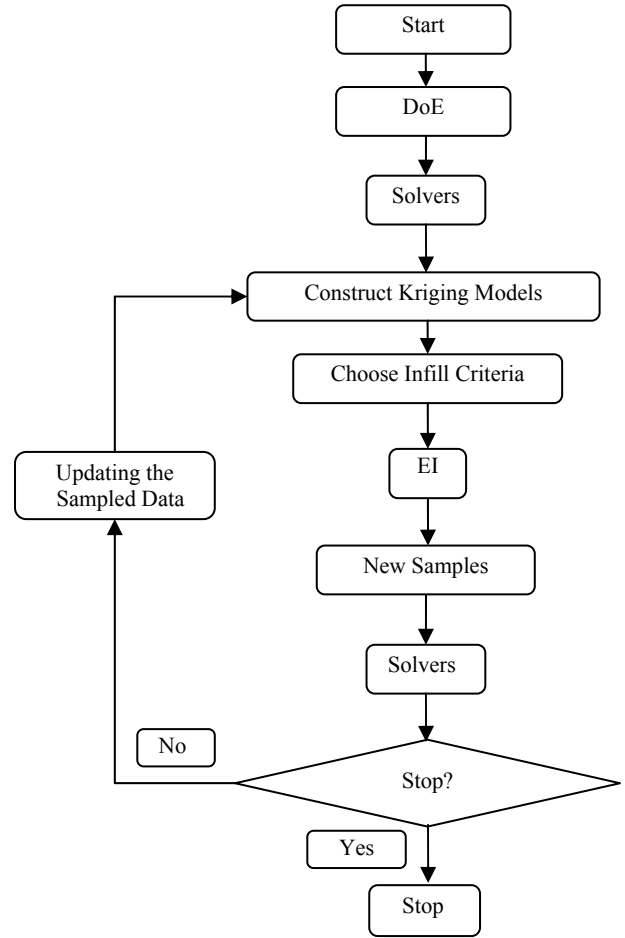


Fig. 9. Framework of the Optimization Platform

4 Results and Discussion

4.1 Validation for RANS Solver

A low Reynolds number propeller test model designed by the research group is investigated. The test model is a two-bladed propeller with a diameter of 1.2 m and a reference chord length of 0.109 m, where $r/R = 75\%$. The aerodynamic performance of the test model is measured in NF-3 low speed wind tunnel of Northwestern Polytechnical University (NPU, China), shown in Fig. 10. The chimera grid system consists of $113 \times 121 \times 149$ H-H type background grid and $225 \times 61 \times 81$ C-H type blade grid. The rotational speed varies from 800 to 2500 rpm with a fixed wind speed of 13 m/s. The definition of Reynolds number is based on the reference chord length and the resultant velocity where $r/R = 0.75$, and the corresponding Reynolds number varies from 2.5×10^5 to 8.0×10^5 .



Fig. 10. Propeller Test Model in NF-3 Low Speed Wind Tunnel

The computed results by different turbulence models with JST as spatial discretization scheme are shown in Fig. 11. Obviously, the results by turbulence models $k-\omega$ SST and S-A are in better agreement with the experimental data for all advancing ratio, and the results by B-L model agree well with the experimental data as the advancing ratio is lower than 0.4, including the design point in this work. Therefore, in this research, B-L model is used to improve computational efficiency.

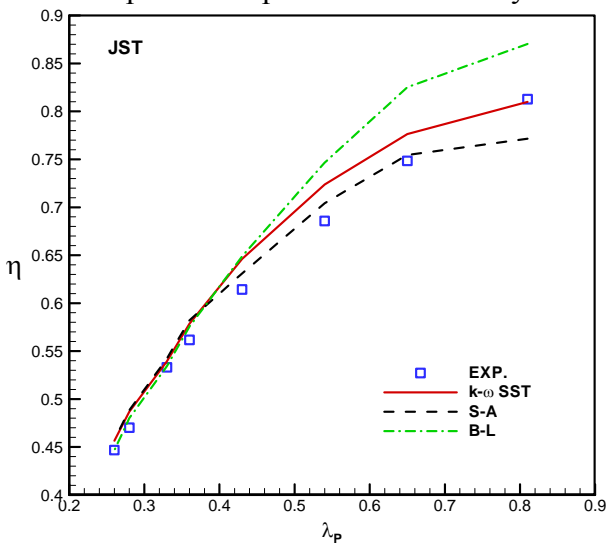


Fig. 11. Comparison of Computed Results and Experimental Data (λ_p - Advancing Ratio, η - Efficiency)

4.2 Optimization of Conventional Propeller

A two-bladed propeller with the diameter fixed to 10m and the absorbing power of 25.5kw is optimized at a single design point (Tab. 1).

Tab. 1. Design Point

Altitude (km)	Wind speed (m/s)	Revolutions per minute (rpm)
20	10	350

The mathematical model of the optimizations is as following:

$$\begin{aligned} & \text{Objective: Maximize } \eta \\ & \text{s.t. : } |P_s - 25.5| < 0.05kw \end{aligned}$$

where P_s denotes absorbing power. An objective function $-\eta$ is used. A Second-order CST formulation is implemented for both chord length and twist angle, thus there are totally 14 variables. Fig. 12 shows the convergent history, the efficiency increases about 2% through the optimization. Fig. 13 and Fig. 14 show the streamlines and pressure contour on the upper surface of the optimized propeller. The streamline demonstrated that there exists separated flow in the inner part ($r/R < 0.4$) of the blade.

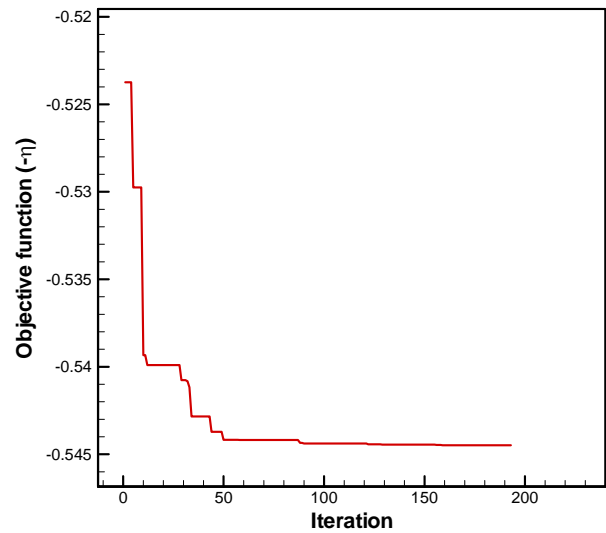


Fig. 12. Convergent History of Optimization

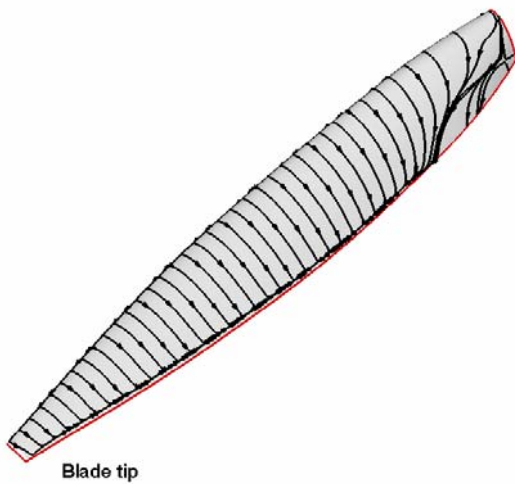


Fig. 13. Streamlines on the Upper Surface of the Optimized Propeller

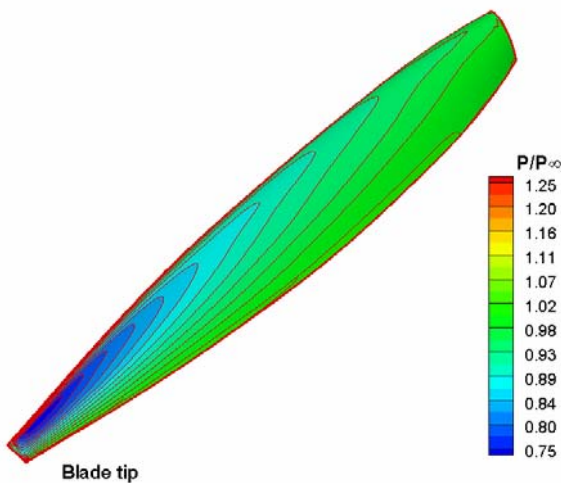


Fig. 14. Pressure Contour on the Upper Surface of the Optimized Propeller

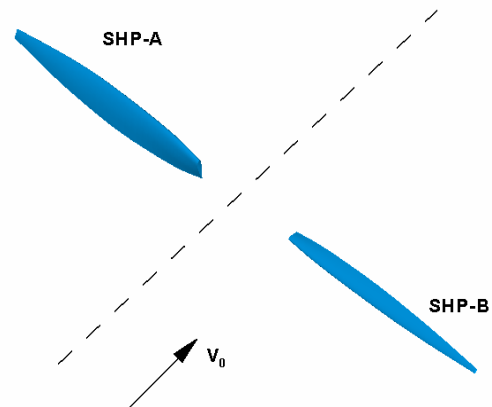


Fig. 15. Conventional Propeller Blade SHP-A and Tandem Propeller Blade SHP-B

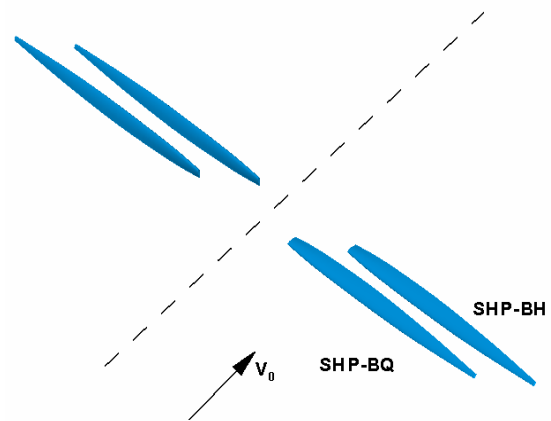


Fig. 16. The Tandem Configuration Propeller (SHP-BQ: Front Propeller, SHP-BH: Rear Propeller)

4.3 Aerodynamic Performance of Tandem Configuration Propeller

Based on the optimized conventional propeller SHP-A, the tandem propeller SHP-B is generated by reducing chord length to half with the same twist angle distribution, shown in Fig. 15. Then a tandem configuration propeller, consists of two SHP-B propellers, is shown in Fig. 16. The front propeller is named SHP-BQ, and the rear propellers named SHP-BH. In present study, the distance between SHP-BQ and SHP-BH is fixed to 1.0 meter.

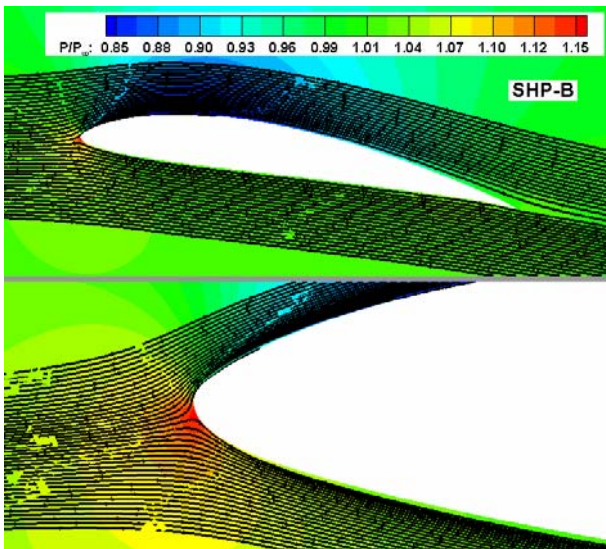
Four configurations are simulated at the design point, including the baseline propeller SHP-A, propeller SHP-B, Tandem-1 and Tandem-2. Compared to Tandem-1, Tandem-2 has an increase pitch angle of 0.9° on the rear propeller to satisfy the constraint of absorbing power.

The aerodynamic performance is list in Tab. 2. Obviously, the computed power of the configuration of Tandem-1 is lower than the absorbing power, and the power of rear propeller SHP-BH is lower than that of front propeller SHP-BQ. Thus, the pitch angle of SHP-BH is increased to reach the absorbing

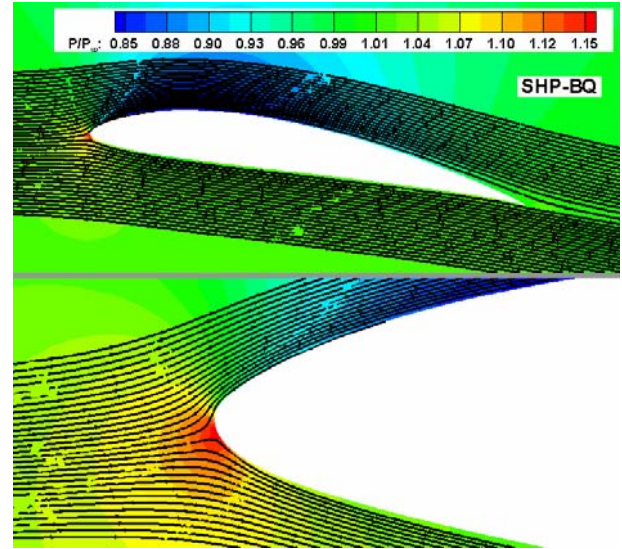
power, named Tandem-2. Compared to the baseline configuration SHP-A, the efficiency of Tandem-2 increases 1.65%, which is an exciting result. Moreover, the efficiency of rear propeller SHP-BH is much lower than that of front propeller SHP-BQ, whereas the absorbing powers are almost the same. The main reason is that rear propeller always works in the slipstream of front propeller, results in a significant decrease in the effective angles of attack and the lift coefficients on the rear propeller, as shown in Fig. 17, although the pitch angle of rear propeller in Tandem-2 is increased.

Tab. 2. Comparison of Aerodynamic Performance between the Conventional and Tandem Configurations

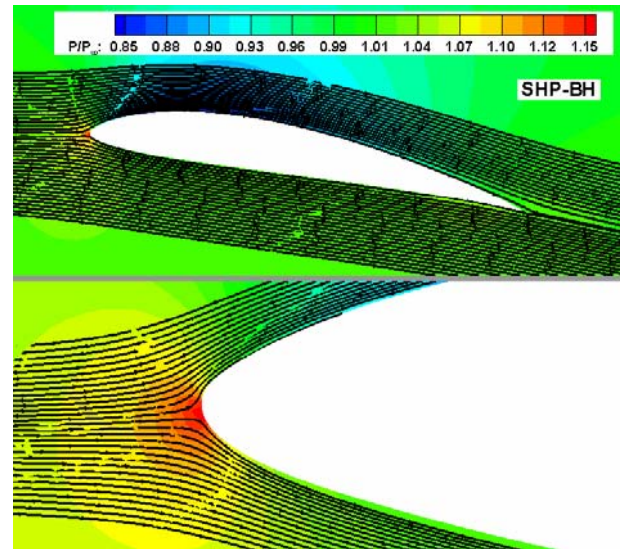
Configurations		T_s (kg)	P_s (kw)	η (%)
SHP-A		141.59	25.48	54.46
SHP-B		78.26	12.40	61.85
Tandem-1	SHP-BQ	77.43	12.46	60.90
	SHP-BH	62.14	11.57	52.63
	Total	139.58	24.04	56.90
Tandem-2	SHP-BQ	77.22	12.48	60.62
	SHP-BH	68.83	13.03	51.78
	Total	146.05	25.51	56.11



(a) SHP-B (Conventional Configuration)



(b) SHP-BQ (Front Propeller in Tandem-2 Configuration)



(c) SHP-BH (Rear Propeller in Tandem-2 Configuration)

Fig. 17. Comparison of Streamlines and Pressure Contours among Different Configurations ($r/R = 75\%$)

5 Conclusions

- (1) RANS solver and GA based on Kriging model are applied to the aerodynamic optimization of low Reynolds number propellers at high-altitude.
- (2) Tandem configuration is helpful to improve the aerodynamic efficiency.
- (3) The efficiency of rear propeller is much lower than that of front propeller, as the slipstream by front propeller resulting in a significant decrease in the effective angles of attack and the corresponding lift coefficients on the rear propeller.

Acknowledgments

The research is funded by the National Natural Science Foundation of China (Grant No. 11302177 & 11272263).

References

- [1] Colozza A. High altitude propeller design and analysis overview, NASA/CR-98-208520, 1998.
- [2] Greer D, Hamory P, Krake K, etc. Design and predictions for a high-altitude (low Reynolds number) aerodynamic flight experiment. NASA/TM-1999-206579, 1999.
- [3] Colozza A. APEX 3D propeller test preliminary design, NASA/CR-2002-211866, 2002.
- [4] Selig M, Guglielmo J and Broeren A, etc. *Summary of low-speed airfoil data - volume 1*. 1st edition, SoarTech Publications, 1995.
- [5] Selig M, Lyon C and Giguère P, etc. *Summary of low-speed airfoil data - volume 2*. 1st edition, SoarTech Publications, 1996.
- [6] Lyon C, Broeren A and Giguere P, etc. *Summary of low-speed airfoil data - volume 3*. 1st edition, SoarTech Publications, 1997.
- [7] Brandt J and Selig M. Propeller performance data at low Reynolds numbers. *49th AIAA Aerospace Sciences Meeting*, Orlando, FL, USA, AIAA Paper 2011-1255, 2011.
- [8] Jameson A, Schmidt W, and Turkel E. Numerical solutions of the Euler equations by a finite volume method using Runge-Kutta time stepping schemes. *14th Fluid and Plasma Dynamics Conference*, Palo Alto, CA USA, AIAA Paper 1981-1259, 1981.
- [9] Xu J H, Song W P, and Han Z H. Calculation of aerodynamic performance of propellers at low Reynolds number based on Reynolds-averaged Navier-Stokes equations simulation. *5th International Conference on Computational Fluid Dynamics*, Seoul, Korea, pp 283-288, 2009.
- [10] Jameson A and Baker T. Multigrid solution of the Euler equations for aircraft configurations. *22nd AIAA Aerospace Sciences Meeting*, Reno, NV, USA, AIAA Paper 84-0093, 1984.
- [11] Baldwin B, Lomax H. Thin layer approximation and algebraic model for separated turbulent flow. *16th AIAA Aerospace Sciences Meeting*, Huntsville, AL, USA, AIAA Paper 1978-257, 1978.
- [12] Spalart P, Allmaras S. A one equation turbulence model for aerodynamic flows. *30th AIAA Aerospace Sciences Meeting & Exhibit*, Reno, NV, USA, AIAA Paper 92-0439, 1992.
- [13] Menter F. Two-equation eddy-viscosity turbulence models for engineering applications. *AIAA Journal*, Vol. 32, No. 8, pp 1598-1605, 1994.
- [14] Yang W Q, Song B F and Song W P. Distance decreasing method for confirming corresponding cells of overset grids and its application. *Acta Aeronautica Et Astronautica Sinica*, Vol. 30, No. 2, pp 205-212, 2009. (In Chinese)
- [15] Mastin C, McConnaughey H. Computational problem on composition grids. *17th Fluid Dynamics, Plasma Dynamics, and Lasers Conference*, Snowmass, CO, USA, AIAA Paper 84-1611, 1984.
- [16] Kulfan M, Bussoletti J. Fundamental parametric geometry representations for aircraft component shapes. *11th AIAA/ISSMO Multidisciplinary Analysis and Optimization Conference*, Portsmouth, VA, USA, AIAA Paper 2006-6948, 2006.
- [17] Kulfan M. A universal parametric geometry representation method – “CST”. *45th AIAA Aerospace Sciences Meeting*, Reno, NV, USA, AIAA Paper 2007-62, 2007.
- [18] Liu J, Han Z H, Song W P. Efficient Kriging-based aerodynamic design of transonic airfoils: some key issues. *50th AIAA Aerospace Sciences Meeting including the New Horizons Forum and Aerospace Exposition*, Nashville, TN, USA, AIAA Paper 2012-0967, 2012.

Contact Author Email Address

Jianhua Xu: xujh@nwpu.edu.cn

Copyright Statement

The authors confirm that they, and/or their company or organization, hold copyright on all of the original material included in this paper. The authors also confirm that they have obtained permission, from the copyright holder of any third party material included in this paper, to publish it as part of their paper. The authors confirm that they give permission, or have obtained permission from the copyright holder of this paper, for the publication and distribution of this paper as part of the ICAS 2014 proceedings or as individual off-prints from the proceedings.